

Article

Coupling Effects of a Top-Hinged Buoyancy Can on the Vortex-Induced Vibration of a Riser Model in Currents and Waves

Chi Yu ¹, Sheng Zhang ² and Cheng Zhang ^{2,*}

¹ Guangdong Energy Group Science and Technology Research Institute Co., Ltd., Guangzhou 510630, China
² School of Marine Science and Engineering, South China University of Technology, Guangzhou 511442, China
* Correspondence: zhangcheng@scut.edu.cn

Abstract: In order to investigate the effects of the top-end dynamic boundary of risers caused by floater motions on their vortex-induced vibration (VIV) characteristics, a combined model comprising a buoyancy can with a relatively simple structural form and a riser is taken as the research object in the present study. The aspect ratios of the buoyancy can and the riser model are 5.37 and 250, respectively. A set of experimental devices is designed to support the VIV test of the riser with a dynamic boundary stimulating the vortex-induced motion (VIM) of the buoyancy can under different uniform flow and regular wave conditions. Several data processing methods are applied in the model test, i.e., mode superposition, Euler angle conversion, band pass filter, fast Fourier transform, and wavelet transform. Based on the testing results, the effect of low-frequency VIM on the high-frequency VIV of the riser is discussed in relation to a single current, a single wave, and a combined wave and current. It is found that the coupling effect of VIM on the riser VIV presents certain orthogonal features at low current velocities. The effect of the cross-flow VIM component on VIV is far more prominent than that of its counterpart, the in-line VIM, with increasing flow velocity. The VIM in the combined wave–current condition significantly enhances the modulation of vibration amplitude and frequency, resulting in larger fluctuation peaks of vibration response and further increasing the risk of VIV fatigue.

Keywords: vortex-induced vibration; dynamic boundary; vortex-induced motion; riser; buoyancy can



Citation: Yu, C.; Zhang, S.; Zhang, C. Coupling Effects of a Top-Hinged Buoyancy Can on the Vortex-Induced Vibration of a Riser Model in Currents and Waves. *J. Mar. Sci. Eng.* **2024**, *12*, 751. <https://doi.org/10.3390/jmse12050751>

Academic Editor: Fuping Gao

Received: 23 March 2024

Revised: 17 April 2024

Accepted: 28 April 2024

Published: 30 April 2024



Copyright: © 2024 by the authors. Licensee MDPI, Basel, Switzerland. This article is an open access article distributed under the terms and conditions of the Creative Commons Attribution (CC BY) license (<https://creativecommons.org/licenses/by/4.0/>).

1. Introduction

Marine risers in offshore oil and gas production systems provide the most critical connection between floating platforms and underwater equipment [1]. The service lives of marine risers are very long in most scenarios, and the fatigue damage is, thus, a significant aspect of their designs. Vortex-induced vibration (VIV), generated through the interactions between the platform, the current, and the riser, is a primary factor that causes fatigue damage to risers. VIV is a typical fluid–structure interaction whose response characteristics are related to both flow states and structural attributes [2,3]. In recent decades, the VIV of marine risers and pipelines immersed in ocean currents has attracted wide concern from researchers and engineers in offshore oil and gas engineering [4–6].

The steady ocean current is often regarded as the dominant factor affecting the VIV of risers and has been investigated in previous studies [7–10]. Steady shear flow is commonly used to characterize the spatial variation in ocean currents. Zhou et al. [11] examined the VIV of a deep-sea riser under bidirectional steady shear flow in a model test. Based on the finite element approach, Jiang et al. [12] examined the two-dimensional VIV and multi-mode responses of fluid-conveying risers in steady shear flow. Besides the steady ocean current, the VIV of a riser system is affected by other complex factors, e.g., floater motions. The surrounding equivalent flow velocity and riser tension are influenced by the combined effect of the floater motion and various marine environmental loads, which undergo time-varying characteristics [13]. The real-time relative flow velocity and the

tension of risers are the critical parameters for VIV. By considering the coupling effect of the overall response caused by the top floater and various marine environmental loads on riser VIV, the study of the unsteady fluid–structure interaction of the riser can contribute to the accurate and systematic understanding of VIV.

In engineering, the flow velocity of ocean currents usually varies on a temporal scale. One of the most common examples is oscillating flow, or the combination of steady and oscillatory flows. Oscillations can be introduced by floating bodies, vessels, or platforms subjected to surface waves. Recently, the riser VIV in oscillatory flow, or subjected to oscillatory forces, has received a lot of attention. Jung et al. [14] conducted an experimental study on the VIV of low-tension submarine cables, in which the flow field was categorized as either uniform flow or a combination of uniform and oscillatory flow. It was observed that there is a periodic enhancement and weakening in the vibration amplitude and frequency under the combined flow, which may contribute to more severe fatigue damage to the structure. By carrying out a dynamic response experiment on a steel catenary riser (SCR), Grant et al. [15] discovered intermittent VIV that was solely excited by the top platform's motion. Wang et al. [16] conducted a systematic experiment on this phenomenon, in which the relative oscillatory currents were achieved by driving the periodic riser motion through a forced motion device. In the article, the relationship between the maximum reduced velocity, the KC number ($KC = U_m \cdot T_f / D$ with U_m and T_f being velocity amplitude and period of oscillatory flow and D being riser diameter), and the riser VIV was also analyzed. Based on the above, Wang et al. [17] conducted an experimental study on the VIV characteristics of an SCR induced by the motion of a floating body on the water surface. The results indicate that in low- KC -number conditions, the time-varying VIV characteristics are highly dependent on the KC number of different pipe positions. Taheri et al. [18] focused on the interaction between oscillatory flow and cylindrical structures in oblique directions and identified different flow regimes affected by structural vibration through numerical simulation. In contrast to the VIV studies focusing on first-mode-dominated flexible pipes in oscillatory flow, Ren et al. [19] investigated the features of a higher-mode-dominated VIV through a model test in the ocean basin. In addition, Neshamar et al. [20] and Deng et al. [21] elaborated on the vibration trajectories of a flexible cylinder in oscillatory flow, which present certain similarities to those of an elastically mounted rigid cylinder under the same conditions.

Some researchers evaluated the effects of a floating body on the riser VIV by exerting excitation directly on the top of the riser. The dynamics of a riser simultaneously affected by the platform sway and VIV were numerically studied by Chen et al. [22]. The displacement level of the riser was found to be amplified several times when platform sway was included in the model. The lateral excitation on the riser top has been used to simulate the sway motion of a platform and has been confirmed to have great effects on VIV; the related results and conclusions are expressed in [23,24]. In terms of the heave excitation on the riser top, Li et al. [25] investigated the VIV of a catenary riser conveying fluid using a semi-empirical model. The effects of double-degree-of-freedom (2DOF) excitations on riser VIV have also been considered. Zhang et al. [13,26] performed a series of model tests on the unsteady VIV of a riser model in uniform flow, affected by single-degree-of-freedom (1DOF) and 2DOF harmonic top-end excitations stimulated by servo motors. They found that the cross-flow (CF) component of the dynamic boundary induces oscillatory characteristics in in-line (IL) VIV, while the IL dynamic boundary component promotes the counterpart of CF VIV. The heave and sway excitations were numerically imposed on the top of a riser by Zhang et al. [27], who found that the combined heave and swing motions result in an increase in CF and IL VIV amplitudes. In order to take the important platform motion into account while evaluating the VIV of a free-hanging riser, Qu et al. [28] modified the wake oscillator by introducing relative oscillatory flow velocity. In addition, Wang et al. [29], Duan et al. [30], and many other researchers have also focused on the motion of floating bodies in VIV studies and suggested that this factor should be considered in VIV response and fatigue evaluation.

Although researchers have gradually identified through various research works that the oscillatory features associated with the dynamic boundaries of floating bodies significantly affect the riser VIV, more specific studies, especially with experimental components, are still at the preliminary stage and introduce many simplifications. For example, the complex platform motions on the riser top are simplified into simple harmonic motions, which leads to a disconnection between the dynamic boundary and the environmental loads. It is difficult to accurately reflect the coupling effect of the riser's dynamic boundary caused by floater motion. Meanwhile, the differences and associations between the CF and IL VIVs affected by multiple-degree-of-freedom dynamic boundaries need to be further clarified. The specific relationships of VIV amplitudes and frequencies with the parameters of dynamic boundaries are also notable issues to be addressed.

In view of the research challenges in VIVs affected by dynamic boundaries, the present study experimentally examines the coupling effects of a top-hinged buoyancy can on the VIV of a riser model in currents and waves. A buoyancy can with a relatively simple circular cylinder structure is selected as the top floating body to generate a top-end dynamic boundary with high recognizability in the current or wave environment. A series of uniform flow, regular wave, and wave–current conditions are designed. The methods of mode superposition, Euler angle conversion, band pass filter, and signal processing, such as fast Fourier and wavelet transforms, are applied to process the testing data. The VIV responses of a riser model, coupled with the vortex-induced motion (VIM) of buoyancy can, are investigated by conducting the model test. By inducing the dynamic boundary of the real structure under different environmental conditions, the relationships between environmental loads, the dynamic boundary, and the riser VIV are discussed. The summarized conclusions for the fluid–structure interaction of VIV are helpful for further understanding complex VIV. The other parts of the paper are organized as follows: The test details are described in Section 2, followed by the experimental data processing in Section 3. In Section 4, the coupling effect of VIM on VIV under uniform currents is discussed, taking the VIVs of three current velocities and two vibration directions into account. Based on this, the influence of waves on the VIV is considered in Section 5, which includes a comparison of the isolated current, the isolated wave, and the combined wave–current. Finally, Section 6 presents the conclusions.

2. Experimental Set-Up

2.1. Test Devices

In this paper, an experiment on the VIV of a riser is conducted at a water basin that is 50 m long, 30 m wide, and 10 m deep. The simulation of uniform flow is formed through the relative movement between a towing carriage and still water, while waves are generated using a wave maker in some cases. The performance of the rocker-flap wave maker covers a wave period of 0.5–4.0 s and produces a maximum wave height of 0.4 m.

The testing devices from our previous study [13] are introduced here as Figure 1. The total testing structure is arranged vertically, with the top end connected to the crane. The bottom end of the riser model is hinged with the lower towing truss. The towing truss height and distance between the left and right steel beams are 6.5 m and 3 m, respectively. The lower part of the riser is connected to the truss by a hinge, and the upper part is hinged to the buoyancy can.

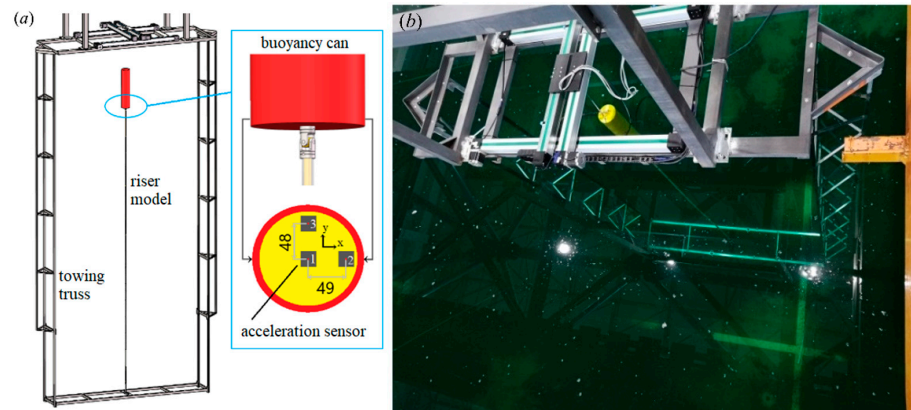


Figure 1. Diagrams of the VIV experimental devices: (a) sketch map and (b) experimental photo [13].

2.2. Test Model

The present riser model is composed of different composite materials, which include copper pipes to provide stiffness, PTFE pipes, waterproof glue, and other auxiliary materials. More details can be found in [26]. The model is shown in Figure 2a.

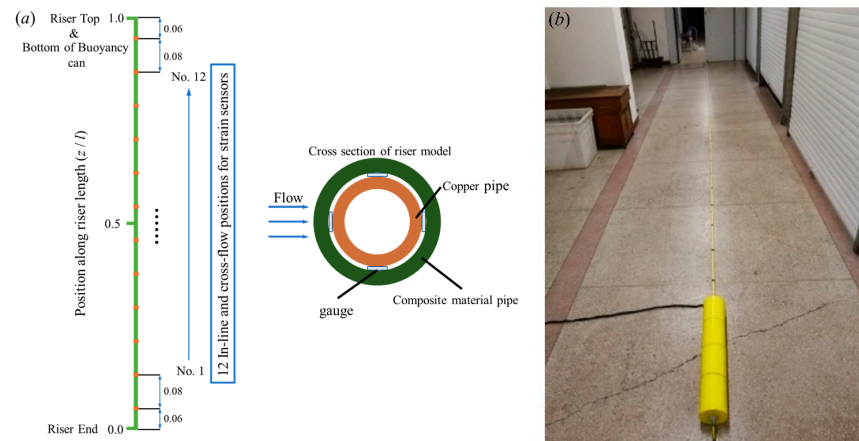


Figure 2. Riser and buoyancy can models: (a) strain gauge arrangement and riser cross-section; (b) picture of the combined model.

In this experiment, strain gauges are applied to measure the strain data along the model. Then, the model displacements of the riser are obtained using the mode superposition method. The arrangement of the strain gauges is displayed in Figure 2b; its design principle refers to [13]. The scale parameters of the composite riser model are described in Table 1. The first six orders of natural frequencies of the riser model tensioned by buoyancy can are listed in Table 2.

Table 1. Riser model parameters.

Aspect Ratio	Length (m)	Outer Diameter (m)	Inner Diameter (m)	Mass Ratio	EI (N·m ²)	EA (N)
250	5	0.02	0.008	2.33	42.62	1.470 × 10 ⁶

Table 2. Natural frequencies of the tensioned riser model.

Order Number	1	2	3	4
Frequency (Hz)	0.993	2.344	4.639	7.666

A regular cylinder made of fiberglass is used as the buoyancy can. It is rigid, water-proof, and divided into four cabins. The lower part of the buoyancy can is hinged on the riser by a cardan joint. Since the aspect ratios of the buoyancy cans in actual free-standing hybrid riser systems are mostly between 4 and 6 [31,32], the experimental model scale was also selected to be in this range. The parameters are listed in Table 3, and a picture of the model can be seen in Figure 2a. The natural frequencies of the riser-hinged buoyancy can in the cross-flow and in-line directions are very close, specifically 0.219 Hz. There are three acceleration sensors arranged inside the buoyancy can. The specific arrangement is exhibited in Figure 1a, where the numerical unit is a millimeter. The 6-DOF motion measurement is obtained through data processing, and the method is described in the next section.

Table 3. Buoyancy can parameters.

Aspect Ratio	Length (m)	Diameter (m)	Displacement (kg)	Mass Iratio
5.37	0.805	0.15	14.23	0.34

2.3. Testing Conditions

The nonlinear top-end dynamic boundary of the riser is the VIM of the buoyancy can. In this experiment, the VIV is investigated in different conditions, involving single uniform flow, single wave, and combined wave–current, respectively. The top of the buoyancy can is nearly 10 mm below the water’s surface under the still water condition. The drifting distance of the buoyancy can significantly increase in large-velocity currents, causing the wires of the measuring instrument to be tightened and further affecting the experiment. Therefore, the flow velocity of the current is kept within the range of 0.1–0.44 m/s, with an interval of 0.02 m/s for different cases. The reduced velocities of the riser model and buoyancy can, represented by U_r and U_{rc} , respectively, are defined as

$$U_r = \frac{U}{f_{n1}D}, U_{rc} = \frac{U}{f_{nc}D_c} \tag{1}$$

where U is the steady flow velocity; D and D_c are the outer diameters of the riser model and buoyancy can, respectively; f_{n1} is the first-order natural frequency of the tensioned riser model; and f_{nc} is the natural frequency of the hinged buoyancy can. The ranges of U_r and U_{rc} are 4.89–21.51 and 3.04–13.39, respectively. The Reynolds numbers corresponding to the riser model and buoyancy can, i.e., Re and Re_c , respectively, are defined as

$$Re = \frac{UD}{\nu}, Re_c = \frac{UD_c}{\nu} \tag{2}$$

where ν is the kinematic viscosity of water. The ranges of Re and Re_c are 2000–8800 and 15,000–66,000, respectively. The wave period range is 1.5–2.5 s, with an interval of 0.5 s. The range of the wave height is 0.1–0.3 m, with an interval of 0.05 m. All of the test conditions are summarized in Table 4. The experimental errors of the vibration strains range from 5% to 20% after multiple replications, which could be caused by the instability of the generated equivalent flow and waves.

Table 4. Wave and flow parameters in different test conditions.

Item	Wave Height (m)	Period (s)	Flow Velocity (m/s)
CM-01-01~CM-01-18	0	0	0.1~0.44
WM-01-01~WM-01-05	0.2	1.5~2.5	0
WM-02-01~WM-02-04	0.1~0.3	2	0
WM-03-01~WM-03-18	0.2	2	0.1~0.44

3. Data Processing

The strain data are directly measured from the experiment. The strain data of a certain model section need to be preliminary processed to separate the VIV strain from the total strain. Then, the strain data need to be converted into time-history displacements. The methods for both the preliminary processing of the strain and the transformation from strain to displacement are very similar to those presented by Zhang et al. [26]; therefore, only a brief summary is presented in the following.

Based on the small deformation assumption, the relationship between the riser model's strain and displacement in matrix form is described by

$$P_{t \times n} = \varepsilon_{t \times m} C_{m \times n}^T \left(C_{n \times m} C_{m \times n}^T \right)_{n \times n}^{-1} / R \tag{3}$$

$$Y_{t \times m} = P_{t \times n} \Phi_{n \times m} \tag{4}$$

where $\varepsilon_{t \times m}$ and $Y_{t \times m}$ represent the strains and displacements in matrix form, m and t are the total number of measure points and the time, $P_{t \times n}$ is a modal weight matrix with n being the modal order, $C_{n \times m}$ is a matrix composed of a modal shape function after a second derivative to length coordinate, $\Phi_{n \times m}$ is the modal shape matrix, and R is the riser radius. The modal weight matrix is computed using Equation (3) based on the strain data and then processed into a displacement matrix through Equation (4).

In addition to the mode superposition method, other approaches are applied to process the experimental data, e.g., band pass filter, Fourier transform, and wavelet transform, and have been validated by Zhang et al. [13,26].

Three acceleration sensors are installed inside the buoyancy can to measure its three-directional accelerations. The acceleration in the local coordinate system, which is moving and rotating with the buoyancy can, can be measured by the sensors fixed on the bottom of the buoyancy can. Then, the motion of the buoyancy can is obtained after Euler angle conversion and integration for the local acceleration. The specific processing method is introduced as follows:

The Euler angle is assumed as $\Theta = [\phi, \theta, \varphi]^T$, where roll, pitch, and yaw are arranged in sequence. The relationship between the acceleration vector a in the local coordinate system and the acceleration vector A in the global coordinate system is described by

$$A = R(\Theta)a \tag{5}$$

where $R(\Theta)$ is the Euler angle conversion matrix:

$$R(\Theta) = \begin{bmatrix} \cos \varphi \cos \theta & -\sin \varphi \cos \phi + \cos \varphi \sin \theta \sin \phi & \sin \varphi \sin \phi + \cos \varphi \sin \theta \cos \phi \\ \sin \varphi \cos \theta & \cos \varphi \cos \phi + \sin \varphi \sin \theta \sin \phi & -\cos \varphi \sin \phi + \sin \varphi \sin \theta \cos \phi \\ -\sin \theta & \cos \theta \sin \phi & \cos \theta \cos \phi \end{bmatrix} \tag{6}$$

The angles of ϕ , θ , and φ can be obtained through

$$\dot{\phi}(t) = \frac{1}{l_{21}} \int_0^t (a_{2z} - a_{1z}) d\tau, \phi(t) = \int_0^t \dot{\phi}(t) d\tau \tag{7}$$

$$\dot{\theta}(t) = \frac{1}{l_{31}} \int_0^t (a_{3z} - a_{1z}) d\tau, \theta(t) = \int_0^t \dot{\theta}(t) d\tau \tag{8}$$

$$\dot{\varphi}(t) = \frac{1}{l_{21}} \int_0^t (a_{2x} - a_{1x}) d\tau \tag{9}$$

where a_{1z} and a_{1x} are the center point accelerations in the z and x directions, a_{2z} and a_{2x} are the starboard point accelerations in the z and x directions, a_{3z} is the bow point acceleration in the z direction, and l_{21} and l_{31} are the distances between two accelerators. The three-directional accelerations in the global coordinate system are then obtained through Equations (5) and (7)–(9). Then, the corresponding displacement results are calculated using a high-precision integral.

4. Coupling effects of VIM on VIV under Uniform Flow

When the buoyancy can and riser are immersed in flow, different fluid–structure interaction phenomena can be captured, i.e., low-frequency VIM and high-frequency VIV. The effect of the low-frequency 2DOF VIM of the buoyancy can on the high-frequency VIV of the riser is discussed in terms of low flow velocity. A comparative analysis is first carried out on the buoyancy can’s VIM features, such as amplitude and frequency. On this basis, the role of the VIM frequency in the riser’s VIV is qualitatively discussed.

4.1. VIM Characteristics of the Buoyancy Can

The effect of the planar motion of buoyancy on VIV is investigated in this paper. The experimental results of the buoyancy can are filtered to eliminate the high-frequency motions of pitch and roll and obtain the planar VIM. Figure 3 shows the VIM results of the buoyancy can in the cross-flow and in-line directions at three flow velocities, i.e., 0.14 m/s, 0.26 m/s, and 0.44 m/s, respectively. The results include time-history motion, FFT spectral density curves, and motion trajectories in two directions. The system identification method is applied to improve the recognition of the motion trajectory [33].

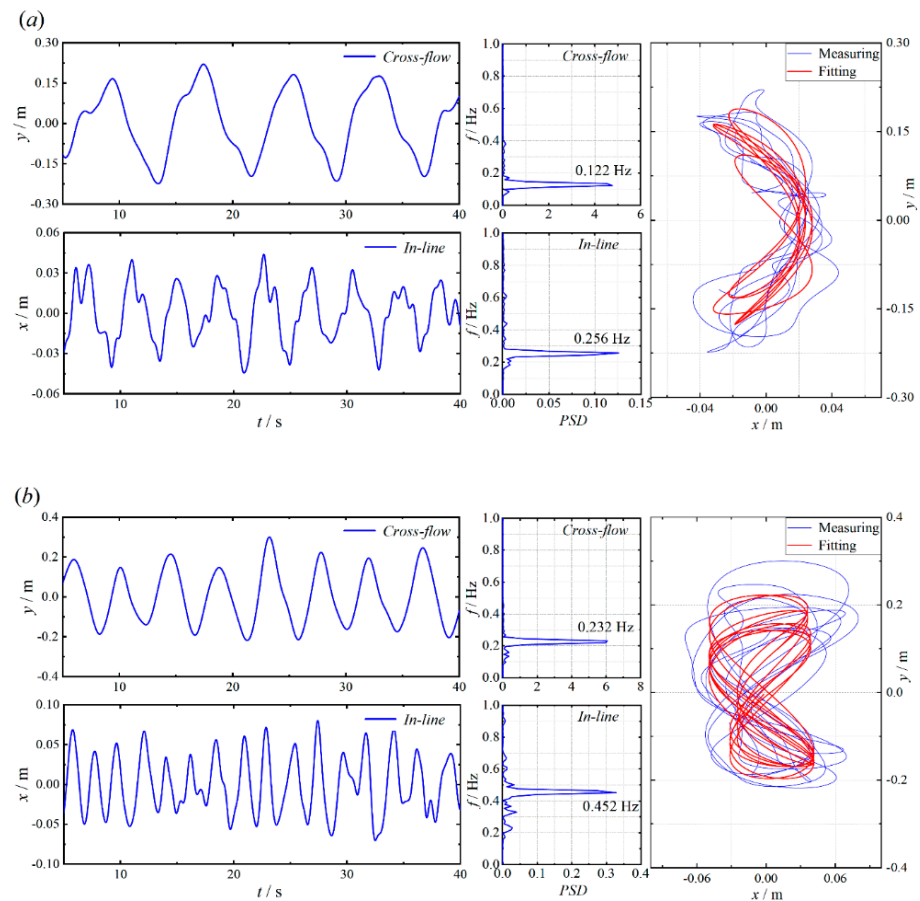


Figure 3. Cont.

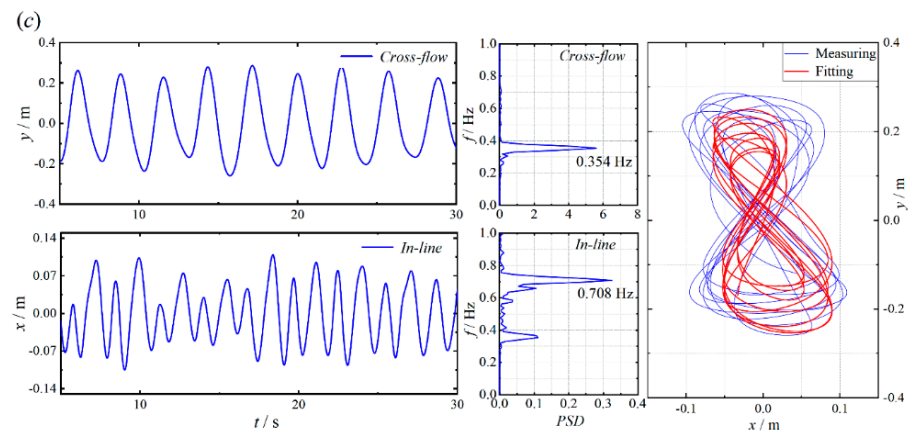


Figure 3. Time–history displacements, FFT frequencies, and motion trajectories of the buoyancy can at different velocities: (a) $U = 0.14$ m/s, (b) $U = 0.26$ m/s, and (c) $U = 0.44$ m/s.

It is observed that the cross-flow motion of the buoyancy can is obvious even at the low flow velocity condition of $U = 0.14$ m/s, and its main frequency is 0.122 Hz. The in-line motion is relatively small, but its frequency is approximately two times higher than that of its cross-flow counterpart, which follows the typical fluid–structure interaction law. There is a phase difference of $\pi/2$ between the cross-flow and in-line motions, which leads to the trajectory changing to a crescent shape. At the medium flow velocity condition of $U = 0.26$ m/s, the amplitudes and frequencies of motions in the two directions present a growing trend when compared with the case at low flow velocity. The in-line and cross-flow motion frequencies are 0.452 Hz and 0.232 Hz, respectively, which maintain a near-twice relationship. Their motion trajectories appear in an “8” shape. When $U = 0.44$ m/s, the amplitudes and frequencies of the in-line and cross-flow motions continue to increase, and the motion frequencies in the two directions reach 0.354 Hz and 0.708 Hz, respectively. The motion trajectories evolve into a relatively standard “8” shape. Kang et al. [33,34] observed an “8”-shaped motion trajectory at medium to high flow velocities in a VIM experiment of a line-tethered buoyant can, which is similar to the results in this paper.

The above analysis shows that most of the motion trajectories of the buoyancy can under medium to high flow velocities are in an “8” shape. The maximum amplitude range of the buoyancy can’s cross-flow motion is 0.1 m–0.3 m, and the motion frequency ranges from 0.1 Hz to 0.35 Hz. The frequency of the in-line motion is double that of the cross-flow. The parameters selected in the present experiment are generally reliable and helpful for studying the impact of VIM boundaries on VIV.

The root mean square (RMS) amplitude and frequency of the buoyancy can displacement at different reduced velocities are shown in Figure 4 to further analyze the amplitude and frequency features of the VIM. As a comparison, the experimental VIM results of Kang et al. [33,34] for a buoyancy can are also presented. In their study, a thin line with a length of nearly 3 m is connected with the buoyancy can [33,34]. The buoyancy can in the present study is hinged with a 5 m riser model. The two restriction methods cause differences in the response of the buoyancy can.

The amplitude and frequency results obtained in this study show a similar trend to those in the literature, indicating the reliability of the experiment. There are also some differences for some values, which are caused by the different testing parameters. The VIM amplitude first grows with increasing U_r , and local peaks appear at $U_{rc} = 5.5$ and 4.3 for cross-flow and in-line VIMs, respectively. After an interval of decreasing amplitude, ending at $U_{rc} = 6.7$, the cross-flow VIM presents continuous growth with a rising U_{rc} . The amplitude of the typical VIV for a cylinder usually presents a falling trend with increasing reduced velocity, defined as the lower branch by Williamson and Govardhan [35]. However, once the mass ratio of the cylinder is below a certain critical value, the vibration amplitude will not decrease at larger, reduced velocities; instead, it will continuously increase [35].

This statement may help to explain the VIM amplitude feature of the buoyancy can due to the similarity of the structure shape and the common point in fluid–structure interaction. A mass ratio of 0.34 was measured for the buoyancy can, which is small enough for many fluid–structure interaction scenarios; thus, the motion presents a higher amplitude at larger U_{rc} . It is found that the present results are close to those of Kang et al. in terms of the VIM frequency [33,34], and there is no obvious lock-in phenomenon. The planar motions of the buoyancy can are coupled with roll and pitch. When the resonance of cross-flow or in-line motion occurs, the roll and pitch may absorb the energy and disturb the resonance, which makes it hard to present a lock-in phenomenon. The cross-flow motion approaches the natural frequency of the buoyancy can in the vicinity of $U_r = 7.3\text{--}7.9$, which is larger than $U_r = 5.5$, corresponding to the amplitude peak that may be caused by the effect of added mass. The variation in f_y/f_{ny} versus U_{rc} is close to the frequency line of $St = 0.16$, which features the vortex shedding frequency. The frequency ratio of the cross-flow and in-line motions is near 2, inducing the “8”-shaped motion trajectory [36].

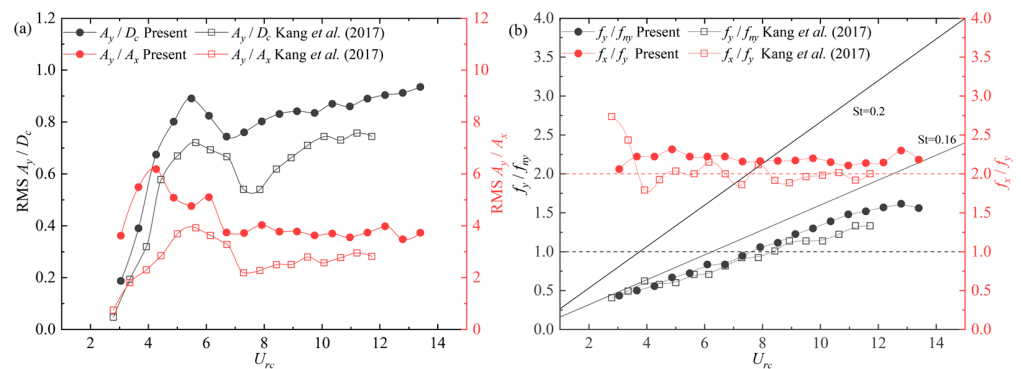


Figure 4. VIM of the buoyancy can: (a) RMS amplitude and (b) primary frequency [33,34].

4.2. VIV Responses Coupled with VIM

The VIV amplitudes and frequencies of the present riser model with the hinged buoyancy can under steady current were discussed in our previous study [26], which can provide a basic reference. The relative velocity between the riser and its equivalent flow oscillates due to the VIM of the buoyancy can. A coupled analysis of the motions of the two structures is conducted here; its purpose is to reveal the oscillation effects of VIM on VIV. A flow condition of $U = 0.26$ m/s is first selected to examine the specific effects, and the results are illustrated in Figure 5. The left subfigure represents the VIM trajectory of the buoyancy can, as well as the cross-flow and in-line motion periods, where D_c is the diameter of the buoyancy can. The right subfigures exhibit time-history vibration displacements, temporary frequencies, and displacements.

When $U = 0.26$ m/s, the motion trajectory of the buoyancy can presents an asymmetric “8” shape. According to the phase difference analysis of the VIV trajectory by Jauvtis and Williamson [37], the phase difference between the cross-flow and in-line VIM is approximately within the range $0\text{--}\pi/4$. Due to the instability of the overall riser vibration under this condition, there is an obvious amplitude modulation phenomenon in the in-line and cross-flow vibrations. It is observed that the overall amplitude modulation periods of the vibration in the two directions are similar, where the value of 4.4 s is close to the cross-flow VIM period. The cross-flow vibration frequency is time-varying near the main frequency of 1.5 Hz, which is smaller than the second-order natural frequency of 2.344 Hz. The natural frequency of the model is obtained from the decaying test in static water, which cannot accurately consider the added mass related to structural acceleration and thus introduces a difference in the frequency. The maximum value of the fluctuation is close to the second-order natural frequency; thus, there are combined first- and second-order features manifested in the vibration mode. The in-line vibration varies intermittently and contains high-order harmonic frequencies. The main frequency is close to the second-order natural frequency, so the in-line mode is in the transitional state from first- to second-order,

but the total amplitude is much lower than that of the cross-flow vibration. At this current velocity, consistently periodic amplitude modulations, time-varying frequency fluctuations, and high-order harmonic phenomena in the riser VIV are induced by the cross-flow VIM. Conversely, the effect of in-line flow VIM is not significant.

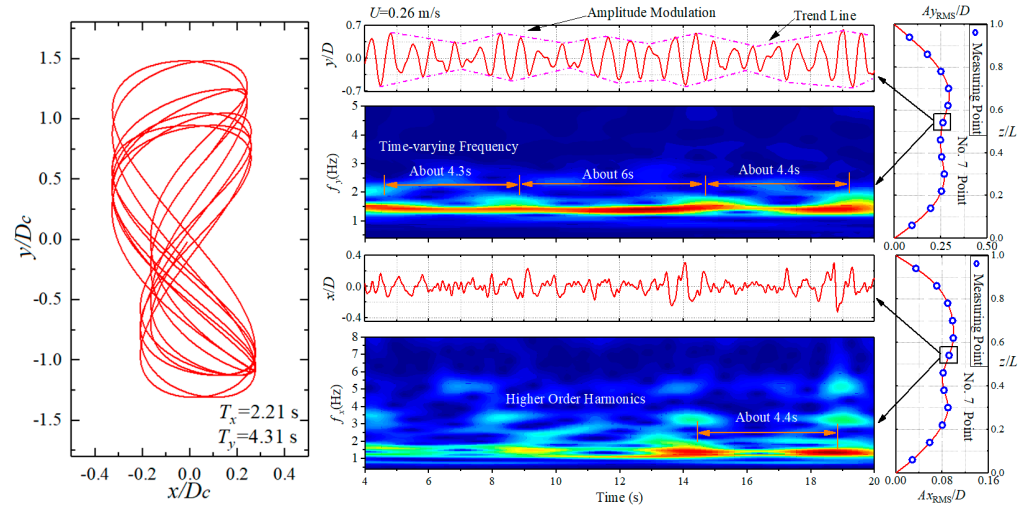


Figure 5. Experimental results of buoyancy can and riser involving time–history displacement, time-varying frequency, and RMS vibration amplitude at a flow velocity of 0.26 m/s.

We presented the results of conditions for other current velocities, i.e., $U = 0.14$ m/s and $U = 0.44$ m/s, in Figures 16 and 17 of Zhang et al. [13]. The results are summarized again in Figure 6 here for comparison and discussion. It is observed that the oscillation period of riser displacement related to the VIM of buoyancy tends to reduce with an increase in flow velocity. The stability of the overall riser vibration is better in the high-velocity condition, while the in-line and cross-flow amplitude modulation is more obvious in the low-velocity state. When $U = 0.14$ m/s, the cross-flow vibration mode is in the first order. As the flow velocity increases, there is a trend of transition from the first to the second order for the cross-flow vibration. The in-line VIM affects the cross-flow VIV more at lower flow velocities, while the cross-flow VIM corresponds to the in-line VIV, which is called an orthogonal coupling effect. As the U rises to 0.44 m/s, the primary and harmonic frequency components, coupled through in-line and cross-flow vibrations, are captured, providing the two-direction coupled feature of VIV. The cross-flow and in-line VIVs are in the second- and third-order states, respectively. In fact, the highest mode detected in this study is the third order, which occurs for in-line vibration at $U = 0.44$ m/s.

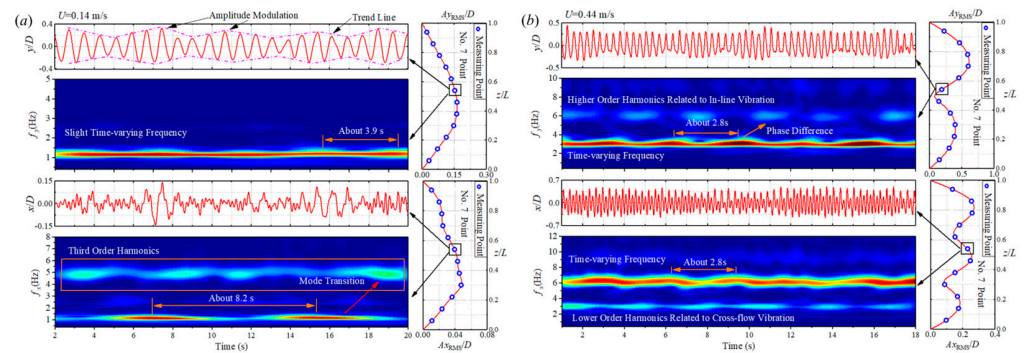


Figure 6. Experimental results of the riser involving time–history displacement, time–varying frequency, and RMS vibration amplitude at (a) $U = 0.14$ m/s and (b) $U = 0.44$ m/s [13].

The results under the three flow velocities are illustrated in Figure 7 to observe the waveform features of the riser vibration affected by VIM. It is found that the cross-flow

vibration presents stronger regularity than the in-line vibration under the three flow velocities. When affected by the VIM, the cross-flow vibration appears as an amplitude variation in the first standing wave at $U = 0.14$ m/s. When $U = 0.26$ m/s, the VIM induces the cross-flow vibration to repeatedly transform between a first-order standing wave and a second-order traveling wave. At a higher flow velocity of 0.44 m/s, the VIV presents a slight amplitude variation in the waveform, even though the VIM is relatively strong. The stability of the in-line vibration waveform is poorer at $U = 0.14$ m/s and $U = 0.26$ m/s. It is observed that the vibration order and amplitude change violently over time, mainly due to the conversion of low-order to high-order waveforms. The periodic features of VIV become prominent at $U = 0.44$ m/s, mainly appearing as a periodic transition between the third-order standing wave in the low-amplitude region and the mixed waveforms of the standing and traveling waves in the high-amplitude region, caused by the periodic velocity oscillation motivated by VIM.

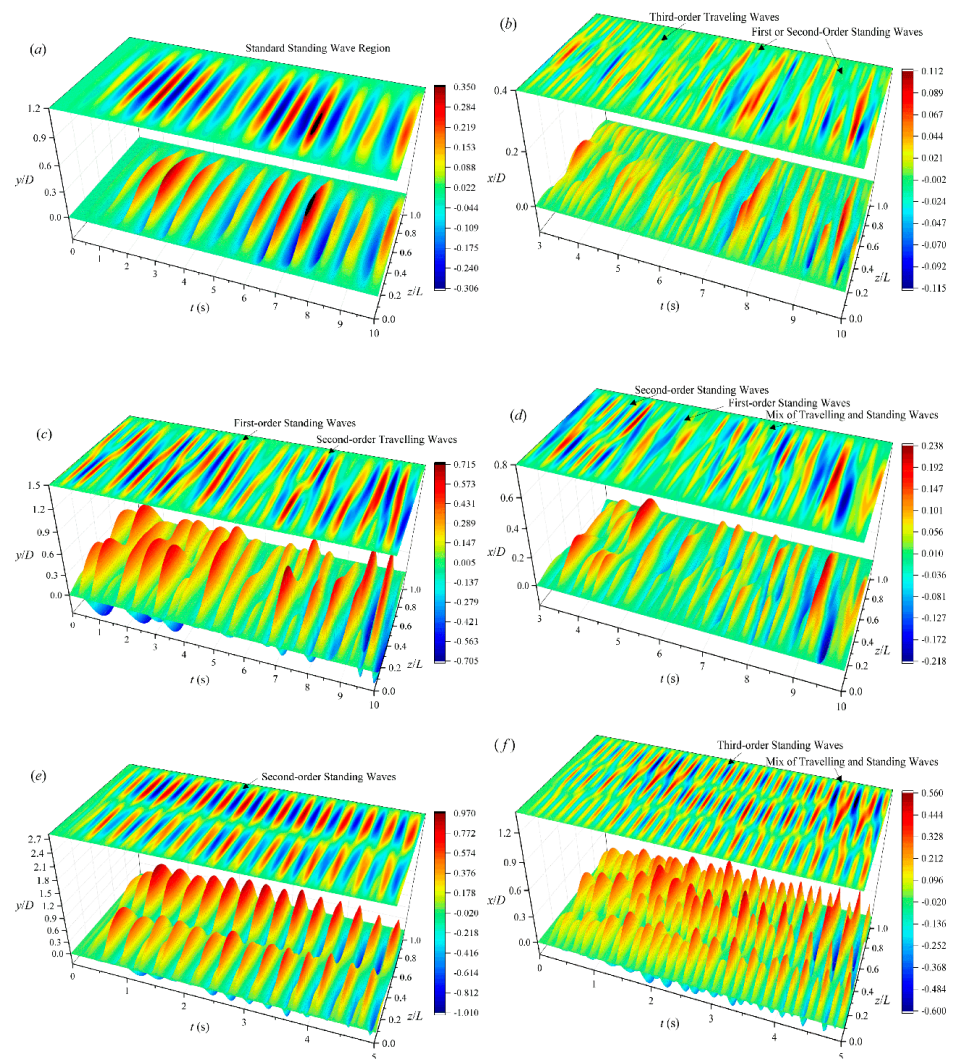


Figure 7. Vibration waveforms at different flow velocities and directions: (a) $U = 0.14$ m/s at cross-flow direction; (b) $U = 0.14$ m/s at in-line direction; (c) $U = 0.26$ m/s at cross-flow direction; (d) $U = 0.26$ m/s at in-line direction; (e) $U = 0.44$ m/s at cross-flow direction; and (f) $U = 0.44$ m/s at in-line direction.

5. Coupling Effects of Wave Load

Waves are one of the most common marine environmental loads acting on floating bodies [38,39]. In the experiment, the whole model is towed in waves, producing the current-wave load. Regular waves are designed in this experiment to investigate the

mechanism more clearly based on the testing results. The parameters of wave height and period are set to 0.2 m and 2 s, respectively. The flow velocity at 0.3 m/s is selected as an example for analysis. The boundary effect of VIM on VIV under the combined wave–current load is discussed here.

The VIM and VIV results of the combined model at different conditions, i.e., isolated current, isolated wave, and combined wave and current, respectively, are depicted in Figure 8. The left-side subfigures show the planar motion trajectories and the motion periods of the buoyancy can; the middle three subfigures present the time-history displacements of the same riser position as Figure 5; and the right-side subfigures show the RMS amplitudes along the riser.

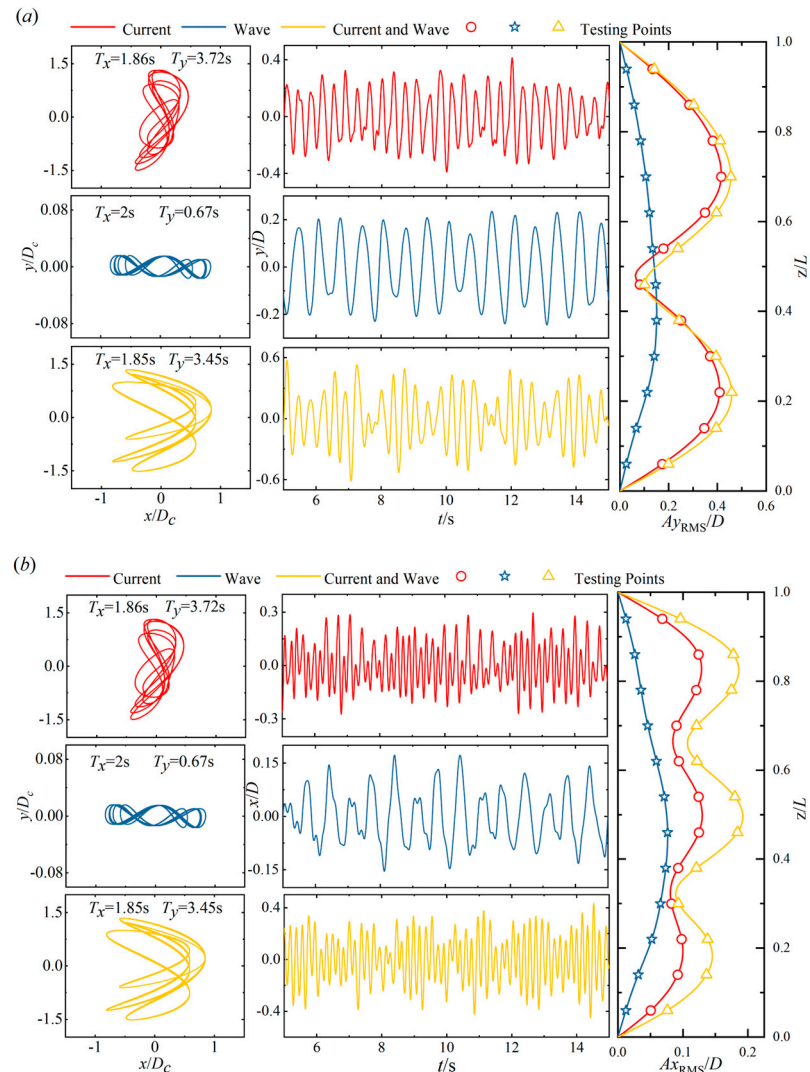


Figure 8. Experimental results under the isolated current, isolated wave, and combined wave and current: (a) cross–flow direction and (b) in–line direction.

When the buoyancy can is immersed in the isolated current or the combined wave and current, it is found to move with a certain “8”-shaped trajectory. When it is only subjected to wave action, the motion trajectory is a flat, woven shape that is very close to a horizontal line. By comparing the amplitude and frequency characteristics of VIM at isolated current and combined wave–current conditions, it is found that the in-line motion amplitude at the wave–current condition is significantly greater than that at the isolated current condition. The cross-flow motion periods are 3.45 s and 3.72 s at the combined wave–current and

isolated current conditions, respectively. This indicates that the waves mainly increase the in-line motion amplitude of the VIM while also reducing the cross-flow VIM period.

Due to the significant influence of the wave on the VIM of the buoyancy can, the coupling between VIM and VIV varies. In the cross-flow vibration condition, the influence of a 1DOF dynamic VIV boundary exhibits an orthogonal effect. When the in-line and cross-flow boundaries coexist with a small difference between them, the former is the dominant effect factor. Under the isolated current, the in-line VIM is much smaller than that of the cross-flow, and the modulation period of the riser VIV amplitude matches that of the cross-flow VIM period. At the combined wave and current state, the wave increases the in-line VIM significantly, which causes a periodic amplitude modulation in the riser VIV, while the period is very similar to that of its in-line counterpart. Similar variation occurs in the in-line vibration, and the wave alters the effect of VIM on VIV. It is found that a first-order riser VIV is excited under the isolated wave when observing the riser RMS amplitude further. The combined wave and current increase the riser VIV amplitude, which is obvious in the in-line VIV.

The vibration frequency is further analyzed. The time–frequency wavelet results under different conditions, i.e., the isolated current, the isolated wave, and the combined wave and current, respectively, are illustrated in Figure 9. Under the isolated current condition, the time-varying fluctuation effect of VIM on the main frequency of the cross-flow VIV (2.61 Hz) is weak. The VIV vibration frequency under isolated waves hardly changes over time. A frequency fluctuation in the cross-flow direction is observed when the two conditions are combined. The fluctuation period is close to the in-line VIM period, while the peak fluctuation exceeds 3 Hz. Although a significant temporal variation feature is exhibited in the in-line VIV under the isolated current condition, the wave characteristics undergo obvious changes. Under the combined wave and current conditions, the fluctuation period becomes shorter and closer to that of the in-line VIM period, while the maximum fluctuation exceeds 6 Hz. The above phenomenon indicates that the oscillation effect of VIM is enhanced by the wave, which leads to higher-order frequencies of the riser VIV.

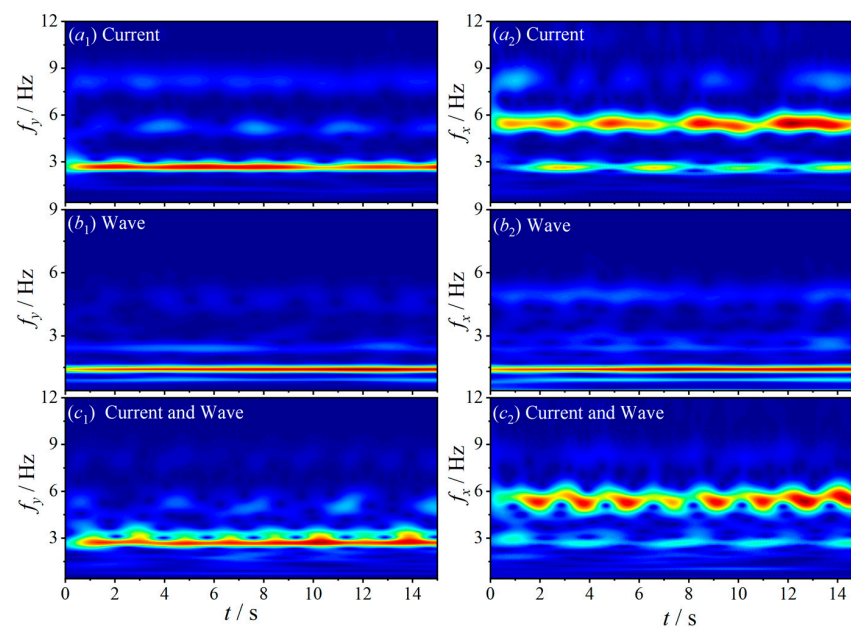


Figure 9. Time-varying frequencies of measuring point No. 7: (a₁) isolated current, (b₁) isolated wave, and (c₁) combined wave and current for cross–flow vibration, while (a₂–c₂) correspond to in–line vibration.

Finally, the riser vibration waveform is analyzed, and the relevant results are shown in Figure 10. Under the isolated current and combined wave–current conditions, the second-order standing wave is the dominant wave of cross-flow vibration, and a locally weak

traveling wave also emerges. Under the isolated wave, the vibration is mainly a first-order standing wave. There is a waveform transition with a period of 2 s, and the wave has relatively little influence on the cross-flow vibration waveform. For the in-line vibration, the vibration waveform under the isolated wave switches between first-order and second-order, and the overall switching period is close to 2 s. Under the combined wave–current and isolated current conditions, both the third-order combined waveform and the third-order standing wave switch periodically, but the switching period of each is different. There is little influence of the wave on the riser vibration waveforms, especially the cross-flow vibration. Moreover, the wave does not change the in-line vibration waveform. However, the switching period of the combined waveform and standing wave varies between the cross-flow VIM period and that of the in-line VIM.

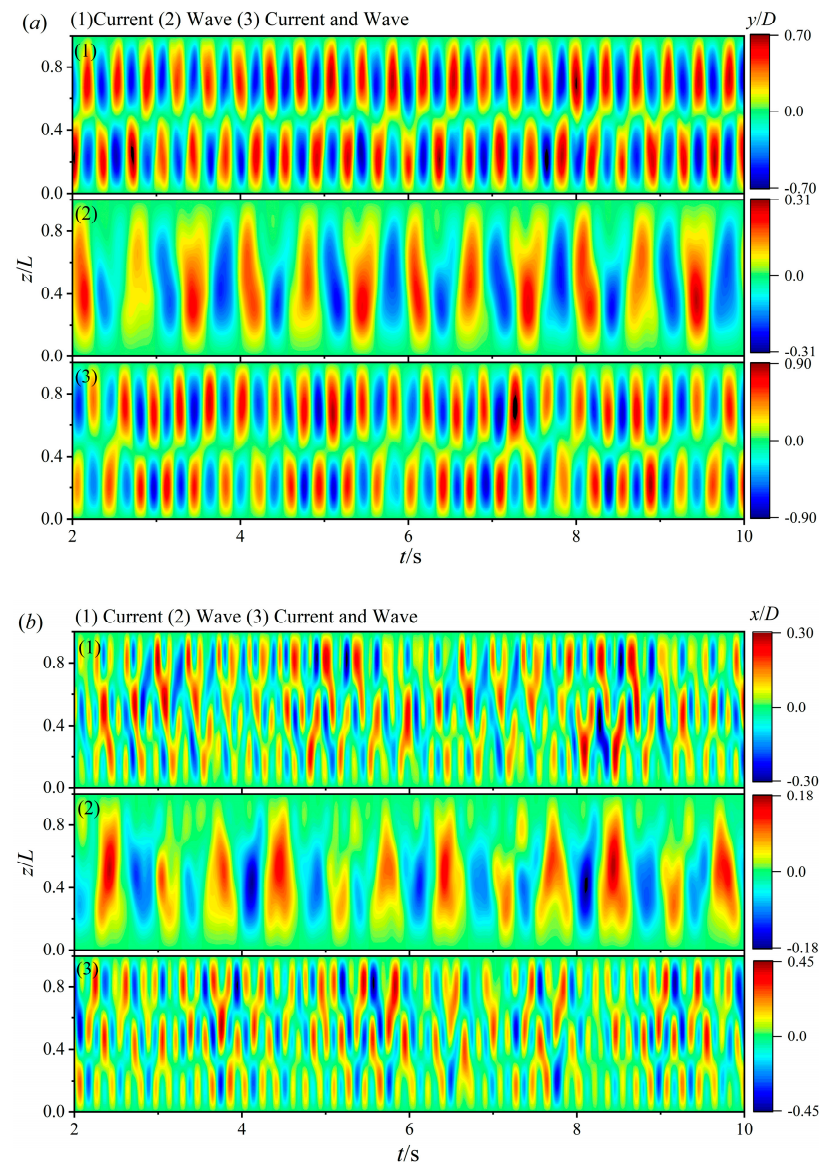


Figure 10. Riser vibrating waveform results under isolated current, isolated wave, and combined wave and current in (a) cross–flow and (b) in–line directions.

6. Conclusions

In this paper, the VIV characteristics of a riser model, hinged with a buoyancy can on top, are experimentally investigated under uniform current and wave conditions. Firstly, the VIM features are analyzed and compared with the literature for validation. The coupling

effects of the buoyancy can's VIM on the riser VIV at different flow velocities are discussed, while the wave is also included in some cases. The following conclusions are drawn:

In terms of the VIM results, the amplitude and frequency results are close to those in the literature, which indicates the reliability of the measurements and data processing in the VIM experiment. The different parameters between the present VIM experiment and those in the literature led to the differences in local values to some extent, which are assumed to be in a reasonable range. Meanwhile, the test set-up and methods were also validated by Zhang et al. (2020, 2022) [26,27], implying that the design of the experiment in the present study satisfies the basic requirements.

The VIM features of the buoyancy can are connected with a riser model, involving the amplitudes, frequencies, and trajectories, which present high similarity to a scenario in which a buoyancy can is moored by a line. This indicates that the small-amplitude and high-frequency VIV have little impact on the large-amplitude and low-frequency VIM of the floater. The VIM may induce low-frequency oscillations in the riser VIV, including periodic modulation of the vibration amplitude, time-varying frequency fluctuations, periodic reproduction of high-order or low-order harmonics, and a switch between the standing wave and the traveling wave. At low current velocity conditions, a certain orthogonal relationship is observed for VIM and VIV. With the increase in flow velocity, this orthogonal effect is no longer significant. The effect of cross-flow VIM on VIV is far more prominent than that of its in-line counterpart.

Waves can significantly amplify the in-line VIM amplitude and allow its in-line component to play a dominant role in the VIV coupling effect. This promotes the oscillation characteristics of VIV, similar to the in-line VIM period. The combined wave–current VIM enhances the amplitude modulation and the overall RMS amplitude of the riser VIV. The time-varying frequency characteristics of VIV are also more obvious in the wave–current condition, resulting in larger fluctuation peaks of frequency. This may further increase the risk of VIV fatigue. The time-scale VIV waveform at the combined wave and current condition is almost consistent with that excited by the isolated current.

Overall, considering the effect of buoyancy can VIM on amplifying the VIV response of the riser model, the dynamic boundary of the platform or the vessel motion should be considered in VIV fatigue assessments when designing risers. In subsequent work, irregular motions of the floating body with more degrees of freedom are expected to be coupled to the top of the risers. This is an area that still needs further investigation. Moreover, further CFD numerical investigations on riser VIV features, especially flow evolutions and hydrodynamic forces, will be helpful for revealing the coupling mechanism of dynamic boundaries with VIV.

Author Contributions: Conceptualization, C.Y. and C.Z.; methodology, C.Z.; software, S.Z.; validation, S.Z. and C.Y.; formal analysis, C.Z.; investigation, C.Z. and C.Y.; resources, C.Y.; data curation, S.Z.; writing—original draft preparation, S.Z.; writing—review and editing, C.Z. and C.Y.; visualization, C.Y.; supervision, C.Z.; project administration, C.Z.; funding acquisition, C.Y. All authors have read and agreed to the published version of the manuscript.

Funding: This research was funded by the Key-Area Research and Development Program of Guangdong Province [grant number 2022B0101100001], the National Natural Science Foundation of China [grant number 52201310], and the Fundamental Research Funds for the Central Universities [grant number D2230600].

Data Availability Statement: We agree to share our research data, which can be obtained by emailing the corresponding author at zhangcheng@scut.edu.cn.

Acknowledgments: We really appreciate Zhuang Kang, who is working at Harbin Engineering University, for providing us with some important experimental equipment during the research.

Conflicts of Interest: Author Chi Yu was employed by the company Guangdong Energy Group Science and Technology Research Institute Co., Ltd. The remaining authors declare that the research was conducted in the absence of any commercial or financial relationships that could be construed as a potential conflict of interest.

References

1. Liu, G.; Li, H.; Qiu, Z.; Leng, D.; Li, Z.; Li, W. A mini review of recent progress on vortex-induced vibrations of marine risers. *Ocean Eng.* **2020**, *195*, 106704. [[CrossRef](#)]
2. Zheng, R.; Wang, C.; He, W.; Zhang, Z.; Ma, K.; Ren, M. The Experimental Study of Dynamic Response of Marine Riser under Coupling Effect of Multiparameter. *J. Mar. Sci. Eng.* **2023**, *11*, 1787. [[CrossRef](#)]
3. Cai, Q.; Li, Z.; Chan, R.W.; Luo, H.; Duan, G.; Huang, B.; Wu, H. Study on the Vibration Characteristics of Marine Riser Based on Flume Experiment and Numerical Simulation. *J. Mar. Sci. Eng.* **2023**, *11*, 1316. [[CrossRef](#)]
4. Chaplin, J.R.; Bearman, P.W.; Huarte, F.H.; Pattenden, R.J. Laboratory measurements of vortex-induced vibrations of a vertical tension riser in a stepped current. *J. Fluids Struct.* **2005**, *21*, 3–24. [[CrossRef](#)]
5. Trim, A.D.; Braaten, H.; Lie, H.; Tognarelli, M.A. Experimental investigation of vortex-induced vibration of long marine risers. *J. Fluids Struct.* **2005**, *21*, 335–361. [[CrossRef](#)]
6. Hong, K.S.; Shah, U.H. Vortex-induced vibrations and control of marine risers: A review. *Ocean Eng.* **2018**, *152*, 300–315. [[CrossRef](#)]
7. Fang, S.M.; Niedzwecki, J.M.; Fu, S.; Li, R.; Yang, J. VIV response of a flexible cylinder with varied coverage by buoyancy elements and helical strakes. *Mar. Struct.* **2014**, *39*, 70–89. [[CrossRef](#)]
8. Wu, J.; Lie, H.; Larsen, C.M.; Liapis, S.; Baarholm, R. Vortex-induced vibration of a flexible cylinder: Interaction of the in-line and cross-flow responses. *J. Fluids Struct.* **2016**, *63*, 238–258. [[CrossRef](#)]
9. Aswathy, M.S.; Sarkar, S. Effect of stochastic parametric noise on vortex induced vibrations. *Int. J. Mech. Sci.* **2019**, *153*, 103–118. [[CrossRef](#)]
10. Zou, X.; Xie, B.; Zang, Z.; Chen, E.; Hou, J. Vortex-Induced Vibration and Fatigue Damage Assessment for a Submarine Pipeline on a Sand Wave Seabed. *J. Mar. Sci. Eng.* **2023**, *11*, 2031. [[CrossRef](#)]
11. Zhou, W.; Duan, M.; Chen, R.; Wang, S.; Li, H. Test Study on Vortex-Induced Vibration of Deep-Sea Riser under Bidirectional Shear Flow. *J. Mar. Sci. Eng.* **2022**, *10*, 1689. [[CrossRef](#)]
12. Jiang, T.; Liu, Z.; Dai, H.; Wang, L.; He, F. Nonplanar multi-modal vibrations of fluid-conveying risers under shear cross flows. *Appl. Ocean Res.* **2019**, *88*, 187–209. [[CrossRef](#)]
13. Zhang, C.; Kang, Z.; Ni, W.; Xie, Z. Coupling effects of top-end dynamic boundary with a planar trajectory of “8” on three-dimensional VIV characteristics. *Mar. Struct.* **2022**, *86*, 103304. [[CrossRef](#)]
14. Jung, D.H.; Park, H.I.; Koterayama, W. A numerical and experimental study on dynamics of a towed low-tension cable. In Proceedings of the ISOPE International Ocean and Polar Engineering Conference, Kitakyushu, Japan, 26–31 May 2002; ISOPE: Mountain View, CA, USA, 2002; p. ISOPE-I.
15. Grant, R.G.; Litton, R.W.; Mamidipudi, P. Highly compliant rigid (HCR) riser model tests and analysis. In Proceedings of the Offshore Technology Conference, Houston, TX, USA, 3–6 May 1999; OTC: Tokyo, Japan, 1999; p. OTC-10973.
16. Wang, J.; Fu, S.; Baarholm, R.; Wu, J.; Larsen, C.M. Fatigue damage induced by vortex-induced vibrations in oscillatory flow. *Mar. Struct.* **2015**, *40*, 73–91. [[CrossRef](#)]
17. Wang, J.; Fu, S.; Larsen, C.M.; Baarholm, R.; Wu, J.; Lie, H. Dominant parameters for vortex-induced vibration of a steel catenary riser under vessel motion. *Ocean Eng.* **2017**, *136*, 260–271. [[CrossRef](#)]
18. Taheri, E.; Zhao, M.; Wu, H. Numerical investigation of the vibration of a circular cylinder in oscillatory flow in oblique directions. *J. Mar. Sci. Eng.* **2022**, *10*, 767. [[CrossRef](#)]
19. Ren, H.; Zhang, M.; Cheng, J.; Cao, P.; Xu, Y.; Fu, S.; Liu, C. Experimental investigation on vortex-induced vibration of a flexible pipe under higher mode in an oscillatory flow. *J. Mar. Sci. Eng.* **2020**, *8*, 408. [[CrossRef](#)]
20. Neshamar, O.E.; O’Donoghue, T. Flow-induced vibration of a cantilevered cylinder in oscillatory flow at high KC. *J. Fluids Struct.* **2022**, *109*, 103476. [[CrossRef](#)]
21. Deng, D.; Zhao, W.; Wan, D. Numerical study of vortex-induced vibration of a flexible cylinder with large aspect ratios in oscillatory flows. *Ocean Eng.* **2021**, *238*, 109730. [[CrossRef](#)]
22. Chen, W.; Li, M.; Zheng, Z.; Guo, S.; Gan, K. Impacts of top-end vessel sway on vortex-induced vibration of the submarine riser for a floating platform in deep water. *Ocean Eng.* **2015**, *99*, 1–8. [[CrossRef](#)]
23. He, F.; Dai, H.; Huang, Z.; Wang, L. Nonlinear dynamics of a fluid-conveying pipe under the combined action of cross-flow and top-end excitations. *Appl. Ocean Res.* **2017**, *62*, 199–209. [[CrossRef](#)]
24. Yuan, Y.; Xue, H.; Tang, W. Nonlinear dynamic response analysis of marine risers under non-uniform combined unsteady flows. *Ocean Eng.* **2020**, *213*, 107687. [[CrossRef](#)]
25. Li, X.; Yuan, Y.; Duan, Z.; Xue, H.; Tang, W. Numerical investigation on vortex-induced vibration of catenary riser conveying fluid under top-end heave excitation. *Ships Offshore Struct.* **2024**, 1–18. [[CrossRef](#)]
26. Zhang, C.; Kang, Z.; Stoesser, T.; Xie, Z.; Massie, L. Experimental investigation on the VIV of a slender body under the combination of uniform flow and top-end surge. *Ocean Eng.* **2020**, *216*, 108094. [[CrossRef](#)]
27. Zhang, B.; Chai, Y.; Li, F.; Chen, Y. Three-dimensional nonlinear vortex-induced vibrations of top-tension risers considering platform motion. *Ocean Eng.* **2022**, *263*, 112393. [[CrossRef](#)]
28. Qu, Y.; Fu, S.; Xu, Y.; Huang, J. Application of a modified wake oscillator model to vortex-induced vibration of a free-hanging riser subjected to vessel motion. *Ocean Eng.* **2022**, *253*, 111165. [[CrossRef](#)]

29. Wang, J.; Jaiman, R.K.; Adaikalaraj, P.F.B.; Shen, L.; Tan, S.B.; Wang, W. Vortex-induced vibration of a free-hanging riser under irregular vessel motion. In Proceedings of the International Conference on Offshore Mechanics and Arctic Engineering, Busan, Korea, 18–24 June 2016; American Society of Mechanical Engineers: New York, NY, USA, 2016; Volume 49934, p. V002T08A040.
30. Duan, J.; Zhou, J.; Wang, X.; You, Y. Vortex-induced vibration of a flexible fluid-conveying riser due to vessel motion. *Int. J. Mech. Sci.* **2022**, *223*, 107288. [[CrossRef](#)]
31. Kang, Z.; Li, H.; Sun, L.P.; Sha, Y.; Cao, J. Overall design and analysis of free-standing vertical risers. *Ship Ocean Eng.* **2011**, *40*, 154–159.
32. Chen, H.F.; Xu, S.P.; Guo, H.Y. Parametric study of global response behavior of deepwater free standing hybrid risers. *J. Ship Mech.* **2011**, *15*, 996–1004.
33. Kang, Z.; Ni, W.; Ma, G.; Xu, X. A model test investigation on vortex-induced motions of a buoyancy can. *Mar. Struct.* **2017**, *53*, 86–104. [[CrossRef](#)]
34. Kang, Z.; Ni, W.; Zhang, L.; Ma, G. An experimental study on vortex induced motion of a tethered cylinder in uniform flow. *Ocean Eng.* **2017**, *142*, 259–267. [[CrossRef](#)]
35. Williamson, C.H.K.; Govardhan, R. A brief review of recent results in vortex-induced vibrations. *J. Wind Eng. Ind. Aerodyn.* **2008**, *96*, 713–735. [[CrossRef](#)]
36. Liu, D.; Ai, S.; Sun, L.; Soares, C.G. Vortex-induced vibrations of catenary risers in varied flow angles. *Int. J. Mech. Sci.* **2024**, *269*, 109086. [[CrossRef](#)]
37. Jauvtis, N.A.; Williamson, C.H.K. The effect of two degrees of freedom on vortex-induced vibration at low mass and damping. *J. Fluid Mech.* **2004**, *509*, 23–62. [[CrossRef](#)]
38. Guo, X.; Fan, N.; Zheng, D.; Fu, C.; Wu, H.; Zhang, Y.; Song, X.; Nian, T. Predicting impact forces on pipelines from deep-sea fluidized slides: A comprehensive review of key factors. *Int. J. Min. Sci. Technol.* **2024**, *34*, 211–225. [[CrossRef](#)]
39. Guo, X.; Liu, X.; Zheng, T.; Zhang, H.; Lu, Y.; Li, T. A mass transfer-based LES modelling methodology for analyzing the movement of submarine sediment flows with extensive shear behavior. *Coast. Eng.* **2024**, *191*, 104531. [[CrossRef](#)]

Disclaimer/Publisher’s Note: The statements, opinions and data contained in all publications are solely those of the individual author(s) and contributor(s) and not of MDPI and/or the editor(s). MDPI and/or the editor(s) disclaim responsibility for any injury to people or property resulting from any ideas, methods, instructions or products referred to in the content.